Numerical investigations on fluid characteristics around the bottom-fixed aquacultural farm

Can Yang[1], Huaqi Yuan[1], Xiaodong Bai[2,*], Zhibin Hao[1], Yuxin Sun[1], Daqing Wu[1], Lars Johanning[1,3]

[1] Yantai Research Institute of Harbin Engineering University, Yantai 264000, China

[2] Department of Naval Architecture and Ocean Engineering, Tianjin University, Tianjin 300072, China

[3] College of Engineering, Mathematics and Physical Sciences, University of Exeter, Penryn Campus, Penryn, Cornwall, TR10 9FE, UK

Abstract

Offshore aquacultural farms are world widely booming in recent years. The bottom-fixed aquacultural farm gains more and more attention because of the large volume and great strength. This study numerically investigates the fluid velocity distribution characteristic around the bottom-fixed aquacultural farm, which is of great importance for fish welfare and pollutant diffusion. The numerical model is developed based on the porous media model for the nets and the rigid walls for the fixed frame. The k-omega turbulence model and the finite volume method are employed to solve the Navier-Stokes equations. The flow velocity distributions around and inside the farm in the varied current velocity are analyzed. The vertical and horizontal flow velocity distributions in various current directions with different net solidities are investigated in detail. Results demonstrated that the configurations of trusses, vertical and horizontal columns of the farm and the interaction with the nets result in complex velocity distributions inside and around the farm. The velocity attenuations at different depths are quite different in uniform and non-uniform currents. The velocity distributions in different attack angles of the flow provide valuable suggestions on the arrangement and layout of the multiple farms.

Keywords: Bottom-fixed aquacultural farm; numerical simulations; velocity distribution; porous media

* Corresponding author.

E-mail address: xdbai@tju.edu.cn (X. Bai).

1 Introduction

Because of the increasing demand for seafood and the overfishing issues, farmed aquaculture becomes more and more important and is projected to be a major supplier of marine proteins to large parts of the global population. The extensive coastal aquacultural activities give rise to great environmental pollutions and reduce the available area. The deteriorated coastal water makes the increase of the production unavailable. It is a world-widely trend that aquacultural fish farms move into the offshore area for improving yields and quality (Chu et al., 2020). However, the traditional net cages made of plastic materials are vulnerable when it is exposed to harsh offshore environmental conditions. For example, the traditional HDPE net cage suffers from structural failure caused by the strong current and wave loads, thus resulting in biomass loss. The large rigid aquacultural structure inspired by the offshore oil and gas industry is a choice. The rigid aquacultural fish farm could stand large environmental loads and can be adapted to the increased dimensions. New types of offshore aquacultural fish farms have been developed recently, such as the semi-submerged aquacultural farm Ocean Farm 1 and Deep Blue 1, the vessel-shaped aquacultural farm Jostein Albert, and the bottom fixed aquacultural farm Genghai 1. The bottom-fixed aquacultural farm (BFAF) is a promising alternative because of the mooring-free configuration and cost-efficient. Particularly, in the Bohai Sea and the Yellow Sea in China where the average water depth is less than 50m even dozens of kilometers far from the coast, BFAF attracts great attention. “Hundred Boxes Project”, no less than one hundred BFAFs installed in those areas, has been planned and carried out in Bohai Sea, China. Several BFAFs as pilots are being fabricated and put into commission, such as Jinghai 1 and Blue Whale 1. To understand the dominating factors for eventual structural failure and biomass loss, it is imperative to investigate the dynamic response of BFAF.

The velocity distribution due to currents is a critical factor for the aquacultural farm. The flow velocity not only influents the structural performance but also involves the fish welfare. The flow velocity around the BFAF also should be considered in the arrangement and layout of the multiple BFAFs. The currents benefit the water exchange, the diffusion of contaminant, and the dissolved oxygen, thus being in favor of fish welfare. Flow velocity reduces when flow passes through the net cages, resulting in low oxygen levels inside than outside the cages. Low velocity inside the BFAF disadvantages the fish growth and should be avoided in the multiple BFAF arrangements. However, the strong currents may cause fish death and increase the environmental loads on the structure leading to structural failure. To ensure structural safety and improve fish welfare, understanding the flow characteristics inside and around the BFAF is required.

The shielding effect and velocity reduction caused by traditional floating net cages and novel aquacultural platforms have been analyzed both numerically and experimentally (Klebert et al., 2013; Xu and Qin, 2020). Løland (1991) proposed a wake deficit model to construct the relationship between

the velocity reduction factor and the drag coefficient in a two-dimensional profile, in which the wakes generated by a screen or a net were a sum of wakes caused by a series of cylinders. However, it is difficult to determine accurate velocity reduction factors by the theoretical formula when the fluid passes through the nets or cage array because of the complicated three-dimensional net structures and interplay between the nets and net structures. Without considerations of the exact geometry of nets, Patursson et al. (2010) incorporated the porous media model with the Reynolds-averaged Navier-Stokes (RANS) equations to simulate the net in currents. The effect of the porous net on the flow is included in the Darcy equations. The resistance coefficients in Darcy equations are obtained by fitting the experimental results of the lift and drag forces on the net panel. Instead of modeling the thousands and thousands of tiny net bars and knots, the porous media model allows the relatively large mesh in CFD modeling and makes the analysis of the flow field available.

Based on the porous media model, Bi et al. (2013) and Zhao et al. (2013a) carried out the PIV experiments to measure the velocity around the undeformed net and numerically investigated the flow velocity reduction of the rigid-net downstream based on the software FLUENT. They further analyzed the effects of angle of attack of the net, net solidities, net knots, and fish on the drag and velocity reductions of the nets (Bi et al. 2014; 2020). To analyze the interactions between the flexible nets and the associated flow around the nets, Chen and Christensen (2017) built the iteration algorithm between the lumped-mass structural model and the porous media model, in which the deformations and the velocity around the nets are investigated numerically and experimentally. Martin et al. (2020) calculated the forces on nets by the screen force model (Kristiansen and Faltinsen, 2012) and distributed the forces on the mesh points. The coupled simulations of the nets and fluid flow were solved based on the numerical framework of the open source CFD solver REEF3D. Gansel et al. (2018) carried out field measurements on velocity reductions and the drag forces on a net cage by towing the cage system in a realistic sea and encouraged more additional experiments to predict the flow velocities inside net cages. Recently, the semi-submersible aquaculture platform and mobile floating aquaculture platform in uniform currents are investigated (Zhao et al, 2021; Martin et al, 2021) with considerations of the rigid structures and porous nets. However, there is less research on the flow field of BFAF. The details of the flow field around the BFAF in currents are rarely investigated with considerations of the complex configurations of BFAF which consist of columns, braces, and nets.

To predict flow velocity inside and around the BFAF in currents, numerical investigations are carried out in this paper. The following context is structured as follows: Section 2 presents the numerical method and several validations. In Section 3, the validated numerical model is applied to BFAF and the flow characteristics are analyzed. The paper concludes with the final remarks in section 4.

2 Methodology

2.1 Numerical modeling

The deformations of the nets are assumed to be negligibly slight because the side and bottom nets are stretched and mounted on the rigid frame. The nets are modeled as porous media. The main frame is modeled by rigid walls. The finite volume method is employed to solve the RANS equations with the shear stress transport k-omega (SST k–ω) turbulence model. The governing equations are discretized using the finite volume method and are solved using the software STAR-CCM+.

The continuous equations and momentum equations are used to describe the movement of fluids inside and around the cage under the action of the currents.

Continuity equation：

$$\frac{\partial \rho}{\partial t}+\frac{\partial(\rho u_i)}{\partial x_i}=0 \tag{1}$$

Momentum equation：

$$\frac{\partial(\rho u_i)}{\partial t}+\frac{\partial(\rho u_i u_j)}{\partial x_j}=-\frac{\partial P}{\partial x_i}+\rho g_i+\frac{\partial}{\partial x_j}(\mu+\mu_t)(\frac{\partial u_i}{\partial x_j}+\frac{\partial u_j}{\partial x_i})+S_i \tag{2}$$

where t is the time, ρ is the fluid density, μ is the fluid dynamic viscosity, μ_t is the eddy current viscosity, $P=p+2\rho k/3$, p is the pressure, k is the turbulent kinetic energy, μ_i and μ_j are the time mean of fluid velocity components, g_i is the gravitational acceleration, i, j=1, 2, 3 represent coordinate components. S_i is the source term of the momentum equation.

The coefficient of porous media is obtained by fitting the pressure drop corresponding to different flow velocities with the least square method. The pressure drop is specified as follows:

$$\Delta p=-\rho(\alpha|v_n|+\beta)v_n \tag{3}$$

where v_n is the superficial velocity normal to the surface, α is the porous inertial resistance, β is the porous viscous resistance. It is based on the formula (also known as nonlinear permeability law) proposed by Forchheimer in 1901 according to Darcy law.

A momentum source term S_i is added to the momentum equation of porous media calculation to act as resistance. In the fluid region outside the porous medium, the source term of momentum equation S_i is set to 0; For the porous media, the source term S_i includes the viscous resistance and the inertial resistance in the following forms (Zhao et al. 2013b):

$$S_i=-\sum_{j=1}^{3}D_{ij}\mu v_j-\sum_{j=1}^{3}C_{ij}\frac{1}{2}\rho|v|v_j \tag{4}$$

where D_ij is the viscosity coefficient matrix. C_ij is the inertia coefficient matrix.

The matrix in equation (4) is replaced by coefficients to obtain the following relation:

$$S_i=-(\frac{\mu}{\partial}v_j+C_2\frac{1}{2}\rho|v|v_j) \tag{5}$$

where 1/α is the viscous resistance coefficient and C_2 is the inertia resistance coefficient.

The coefficient of porous media is determined by the geometry and configurations of nets, which can be obtained by the experiments. The measured flow velocity and the resistance value are general fitted by using the least square method when the corresponding velocity flows through the porous media area. The resistance force F_d and lift force F_l are obtained through physical experiments, and can also be calculated through the Morison equation:

$$F_d = 0.5\rho C_d A|u|^2 \tag{6}$$

$$F_l = 0.5\rho C_l A|u|^2 \tag{7}$$

where C_d is the resistance coefficient, C_l is the lift coefficient, which can be calculated using empirical formulas proposed by Løland (1991).

When the flow direction is perpendicular to the net (attack angle is 90°), the lift forces value is 0 and D_t and C_t can be ignored. According to Bear (1972) for the flow direction and the net reach a certain attack angle α, the porous media coefficient should be transformed based on the following formula:

$$D'_n = \frac{D_n + D_t}{2} + \frac{D_n - D_t}{2}\cos(2\alpha') \tag{8}$$

$$C'_n = \frac{C_n + C_t}{2} + \frac{C_n - C_t}{2}\cos(2\alpha') \tag{9}$$

$$D'_t = \frac{D_n - D_t}{2}\sin(2\alpha') \tag{10}$$

$$C'_t = \frac{C_n - C_t}{2}\sin(2\alpha') \tag{11}$$

where α′=90°-α, α is the attack angle. The optimal porous media coefficients can be obtained by fitting the experimental value and the theoretical value based on the least square method.

The SST k-ω model (Menter, 1994) is used in this study, which is widely used in aerospace and marine industry. Compared with the k-ε model, the boundary layer performance of the k-ω model is changed under the backpressure gradient. The main advantage is that the model can be applied to the entire boundary layer without further modifications. The SST k-ω model effectively blends k-ε model in the far field with the k-ω model in the near wall, thus solving the largest shortcoming of k-ω model in practical fluid simulation.

The transport equations for the kinetic energy k and the specific dissipation rate ω are:

$$\frac{\partial}{\partial t}(\rho k) + \nabla\cdot(\rho k\bar{v}) = \nabla\cdot\left[(\mu + \sigma_k\mu_t)\nabla k\right] + P_k - \rho\beta^* f_{\beta^*}(\omega k - \omega_0 k_0) + S_k \tag{12}$$

$$\frac{\partial}{\partial t}(\rho\omega) + \nabla\cdot(\rho\omega\bar{v}) = \nabla\cdot[(\mu + \sigma_\omega\mu_t)\nabla\omega] + P_\omega - \rho\beta f_\beta(\omega^2 - \omega_0^2) + S_\omega \tag{13}$$

where $\bar{v}$ is the average velocity, μ is the dynamic viscosity, σ_k, and σ_ω, are the model coefficients, P_k and

P_ω are the result terms, $f_{\beta*}$ is the free shear correction factor, f_β is the eddy current extension correction factor, S_k and S_ω are the source terms, k_0 and ω_0 are the environmental turbulence values preventing turbulence attenuation.

Kinematic eddy viscosity is

$$v_T = \frac{a_1 k}{\max(a_1 \omega, SF_2)} \tag{14}$$

Turbulence kinetic energy is

$$\frac{\partial k}{\partial t} + U_j \frac{\partial k}{\partial x_j} = P_k - \beta^* k\omega + \frac{\partial}{\partial x_j}\left[(v + \sigma_k v_T)\frac{\partial k}{\partial x_j}\right] \tag{15}$$

Specific dissipation rate is

$$\frac{\partial \omega}{\partial t} + U_j \frac{\partial \omega}{\partial x_j} = \alpha S^2 - \beta \omega^2 + \frac{\partial}{\partial x_j}\left[(v + \sigma_w v_T)\frac{\partial \omega}{\partial x_j}\right] + 2(1 - F_1)\sigma_{\omega 2}\frac{1}{\omega}\frac{\partial k}{\partial x_i}\frac{\partial \omega}{\partial x_i} \tag{16}$$

where S is the mean strain rate tensor, a_1 is the model coefficient. In the near-wall region, F_1=1, where it equals zero in the outer region. Other constants are given as: a_1 =5/9, β_1=3/40, β_2=0.828, β^*=9/100, σ_{k1}=0.85, σ_{k2}=1, $\sigma_{\omega 1}$=0.5, $\sigma_{\omega 2}$=0.856.

The bottom-fixed aquacultural farm is mainly composed of frame columns, fish nets and supporting trusses. The porous media theory can be used in engineering analysis to simplify the actual aquaculture nets. By reasonably setting the porous medium coefficient and porosity, the same flow resistance effect as the net can be produced by the porous medium. It is considered that the stiffness of the column is large enough so that the deformation caused by the action of water flow can be ignored. Almost all previous studies are based on the model scale, which may result in the scale effect and the unrealistic flow characteristic. To provide a practical reference of the flow characteristic, the prototype farm is simulated in this study. The square aquacultural farm is 40 m height with a 30 m draft as shown in Figure 1. The diameter of the four main vertical columns is 6 m. The height of the base is 3.5 m. The diameter of the upper horizontal truss structure is 1 m and the diameter of the lower horizontal column is 2.5 m.

In the numerical calculation, the finite volume method is used to discretize the governing equations. The governing equations are solved by the pressure-based discrete solver, together with the pressure-velocity coupling selected SIMPLEC algorithm. To improve the convergence rate and the accuracy of the solution, the second-order upwind scheme is adopted for the dispersion of pressure, momentum, turbulent kinetic energy and dissipation rate. The convergence of residuals is calibrated and examined. To ensure sufficient accuracy, the residual values of the continuous equation, turbulent kinetic energy k, and specific dissipation rate ω are set to 0.001. The time step of the solution to 30000 steps can make the numerical calculation reach the predetermined accuracy.

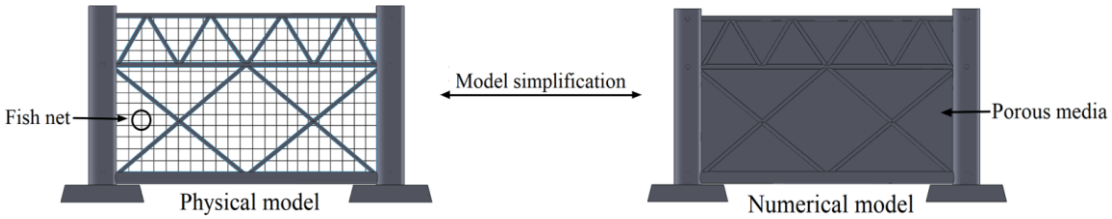

Figure 1. Numerical model of bottom-fixed aquacultural farm.

The grid division of the calculation area of the numerical model adopts the cut volume grid generator, which provides a stable and effective method for simple and complex grids to generate high-quality grids. The fluid area and the BFAF area are included in the entire numerical model, as shown in Figure 2. The basic size of the fluid area grid is 2.4 m and the minimum surface size is 0.24 m. Considering the influence of the near-wall effect, the prism layer should be divided and the prism layer stretching should be 1.3. The basic grid size of the densification zone is 1.2 m. The basic size of the BFAF area grid is 1.4 m and the minimum surface size is 0.14 m. The grid of the frame column is encrypted through the surface control, and the curvature is set to 144 to ensure the geometric characteristics of the cylinder.

Based on the right-handed Cartesian coordinate system, the origin of the coordinate is established on the projection of the center of the aquacultural farm on the water surface, as shown in Figure 3. Define the positive direction of the x-axis as the water flow direction, the y-axis perpendicular to the water flow direction, and the z-axis vertically upward. The left boundary of the numerical flume is defined as the velocity inlet. The right end is defined as the free flow boundary. The side wall of the flume is defined as a symmetrical plane. The bottom of the flume is a wall without slippage. The horizontal plane adopts a wall boundary with shear stress equal to zero. To reduce the influence of the near-wall effect, the wall function method and the boundary layer grid are used to solve the near-wall viscosity influence area.

In the calculation of turbulence using k-ω model, the turbulent kinetic energy k and specific dissipation rate ω of the fluid at the inlet boundary must be specified, which can be calculated as follows (Anderson, 1995):

$$I=0.16(Re_D)^{-0.125} \tag{17}$$

$$k=1.5(UI)^2 \tag{18}$$

$$\omega = C_{\mu}^{-\frac{1}{4}} \frac{\sqrt{k}}{l} \tag{19}$$

where I is the turbulence intensity, Re_D is the Reynolds number obtained from the hydraulic diameter of the flume D_H as the characteristic length, U is the average velocity, l is the turbulence length scale, and C_μ is the turbulence model constant, usually minus 0.09.

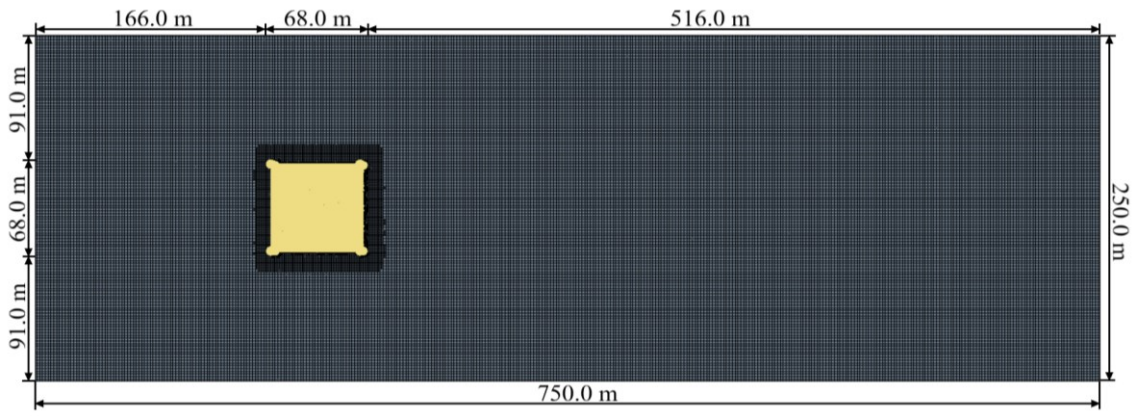

Figure 2. Computational grid for the numerical model.

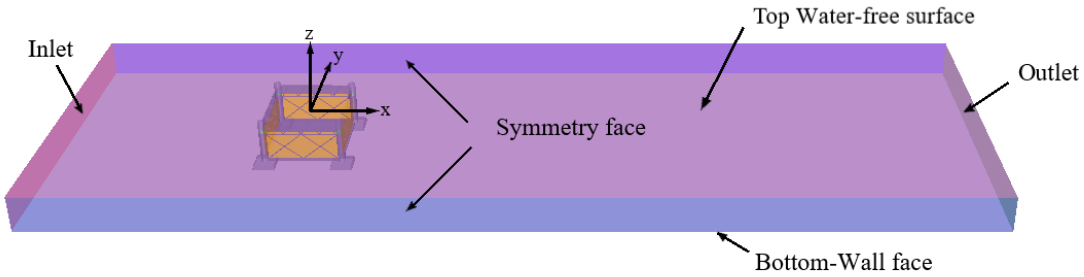

Figure 3. Boundary conditions of numerical models.

2.2 Validation of numerical model

2.2.1 Validation of a plane net perpendicular to the direction of flow

To verify the numerical model, the numerical results of the panel net are compared with the experiments conducted by Zhao et al (2013a). The numerical flume is established with a depth of 0.7 m and a width of 1 m. The plane net is simulated by the porous media sheet with a height of 0.4 m, a width of 1m and a thickness of 50 mm. In Zhao's experiments, the flow velocity and the corresponding resistance were measured. The porous media coefficient was obtained by fitting the least square method. The inertia resistance P_i and viscous resistance P_v of porous media are calculated as 4144.5875 kg/m^4 and 76.37 kg/m^3·s. The flow field was observed at the flow velocities u=0.159 m/s and u=0.3072 m/s.

In the numerical modeling, the tetrahedral grid is used and the fluid domain mesh base size is 0.1m. The minimum surface size is 0.01m. The prism layer is set and the extension factor of the prism layer is 1.3. The mesh base size of the porous media area is 0.025m. The minimum surface size is 0.0025 m and the mesh size of the encrypted area is 0.02m, as shown in Figure 4. Figure 5 shows the location distribution of each measuring point. The net has a certain blocking effect on the flow velocity. It can be found from the numerical and experimental results that the flow velocity from measuring point B to measuring point C has a significant attenuation. The flow velocity at measurement points obtained by numerical simulations is compared with the experimental results as well as numerical results in Zhao et

al (2021). Comparisons are presented in Figure 6. It can be seen that the simulated values are close to the experimental values. For u=0.1590 m/s, the maximum relative difference between the numerical and experimental results is 2.197% and the average relative difference is 1.217%. For u=0.3072 m/s, the maximum relative error is 5.542% and the average relative difference is 2.075%. Comparisons of the numerical results with Zhao's numerical results shows that the present numerical model can give a reasonable estimation of the flow field of the panel net.

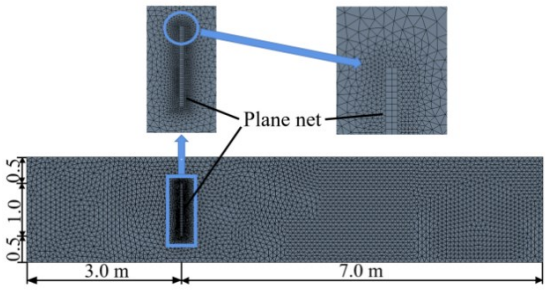

Figure 4. Computing grid for the plane net.

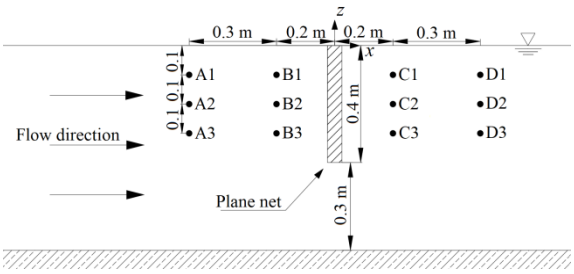

Figure 5. Layout of the measurement points for plane net.

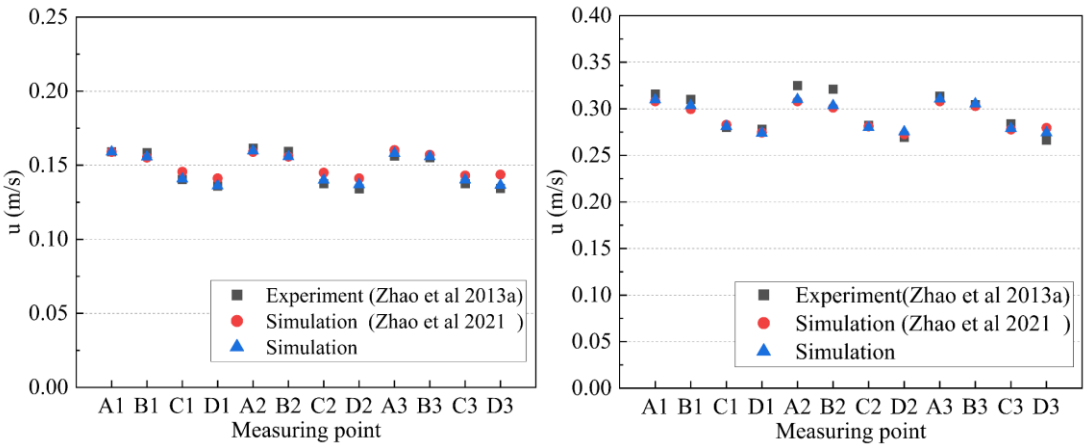

a. Incident velocity 0.1590 m/s b. Incident velocity 0.3072 m/s

Figure 6. Comparison of experimental and numerical results.

2.2.2 Validation of a plane net at different attack angles

In this section, the numerical simulation will be verified by the physical experiment of Bi et al (2013)

and the numerical simulation results of Bi et al (2014). The plane net size is 0.3 m × 0.3 m, fixed by a square frame with a diameter of 6 mm. The deformation of the plane net frame can be ignored. Figure 7 displays the physical model and measuring point position. It should be noted that the inclination angle (θ) describes the angle between plane net and z axis on vertical plane as shown in Figure 8. The origin of the coordinate system is set at the center of the plane net on the water surface. The x positive direction is defined as along the flow direction, y is perpendicular to the horizontal flow direction, and the z is straight upward.

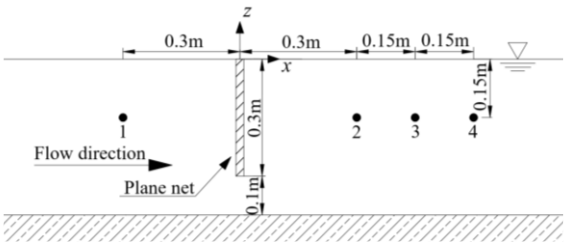

Figure 7. Physical model and measuring point position.

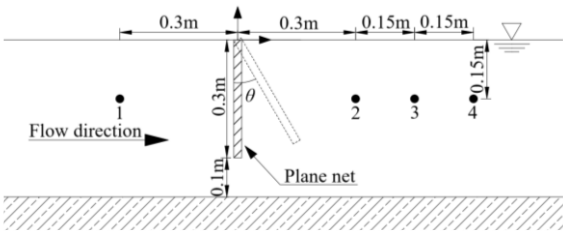

Figure 8. Definition of inclined angle(θ).

The three-dimensional numerical model based on porous media is established according to the physical model. The thickness of 20 mm for porous media is chosen in this simulation. At the boundary of inlet, u_0=0.17m/s is selected as incoming velocity to observe the effect of the plane net. The numerical results compared with the previous results are shown in Figure 9. The maximum relative errors between experimental and simulated results are 1.62% and 1.34%, respectively. These comparisons prove that the flow characteristics of plane net at different attack angles can be well simulated.

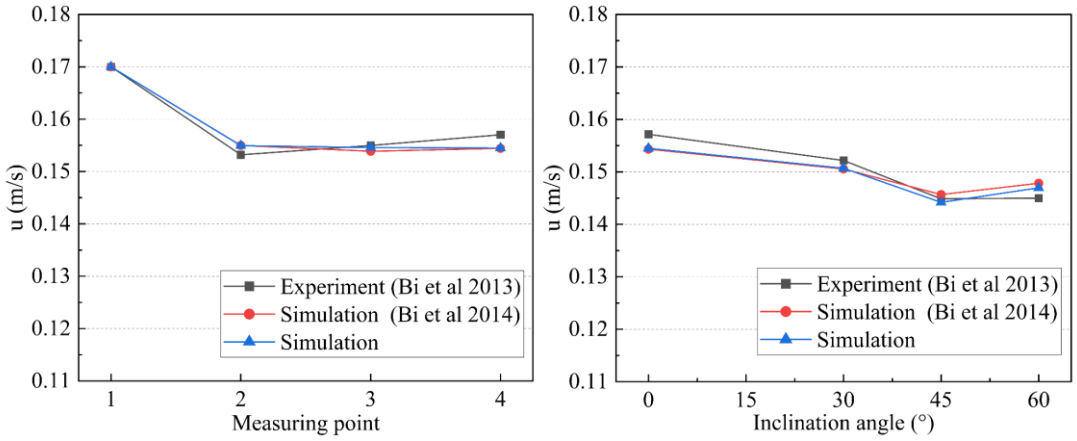

a. b.

Figure 9. Comparison of experimental and numerical results: a. the velocity amplitude at different measuring points, b. the velocity magnitude for different inclination angles at measuring point 4.

2.2.3 Validation of flow characteristics of net cage

The numerical model is validated by comparing the numerical results of the flow field around the net cage with the existing research. The numerical simulation of the flow field inside and around the gravity cage has been studied in Zhao et al (2013b). The calculation model is equivalently simplified by dividing the gravity cage into 16 plane nets with different attack angles. In their simulations, the influence of the net deformation is ignored. The plane nets that make up the gravity cage are calculated using porous media. Figure 10 shows the numerical model and the coordinate system. The origin of the coordinates is established on the projection of the cage center on the water surface. The flow direction is along the positive *x*-axis. The flume is 240m long, 80m wide, the water depth is 20 m and the draft of the cage is 10 m. The diameter of the cage is 16 m and the thickness of the porous medium is 50 mm. The velocity inlet boundary is located 40m upstream from the center of the cage with the designed inflow velocity being u=0.5 m/s.

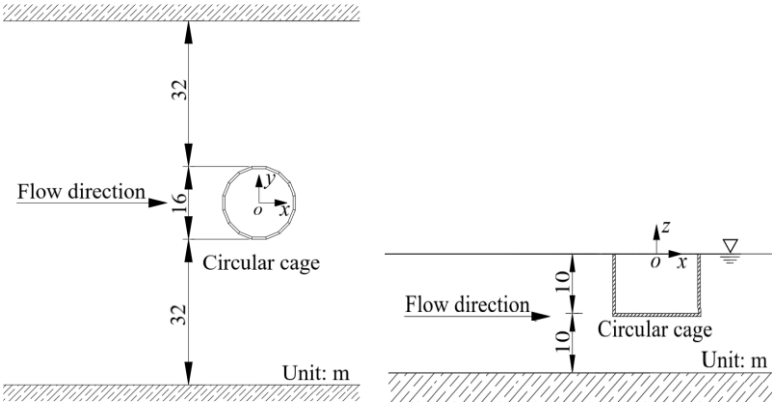

a. Vertical view b. Front view

Figure 10. Sketch of the net cage in numerical simulation.

Comparisons of the flow velocity with the results in Zhao et al (2013b) are displayed in Figure 11.

The magnitudes of the flow velocity v_x at y=0 m along the x-direction and v_y at x=0 m along the y-direction are analyzed. It can be observed that the flow velocity decreases to a stable value in the x-direction after passing through the circular cage. The data demonstrate that the numerical simulation values agree well with the reference values. The maximum relative difference between the numerical results and the reference values are 3.34% and 6.88% for the v_x and v_y, respectively. The average relative errors are more indicative of data reliability, with v_x and v_y being 1.32% and 1.70%, respectively. The relative error is within the allowable value range, indicating the good agreements. In brief, the numerical model can be used to simulate the flow field inside and around the aquacultural farm.

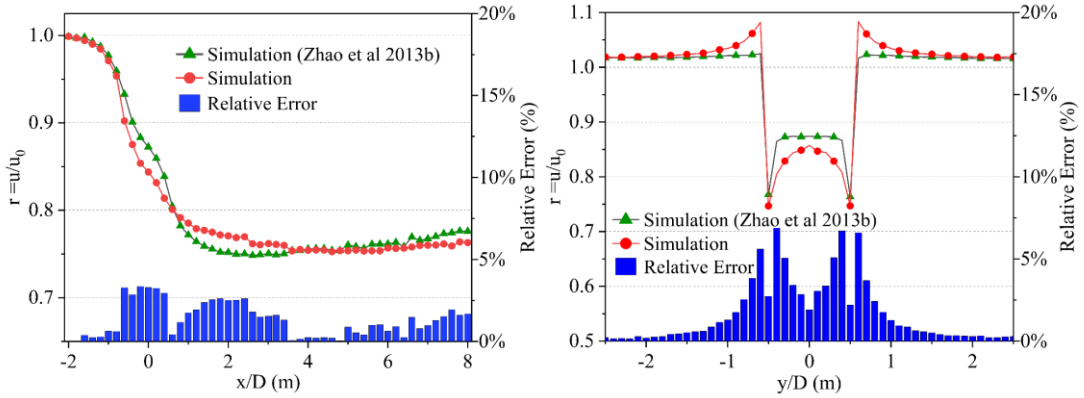

1) y/D=0 2) x/D=0

Figure 11. Comparison of flow velocity between the numerical simulation and results from Zhao et al.(2013b).

3 Result and discussion

3.1 Flow velocity distribution

The flow field distribution inside and around the aquacultural farm is quite complex. To intuitively observe the flow field characteristics around the farm, several different points and slices are selected as shown in Figure 12. The flow field under uniform currents and non-uniform currents are investigated.

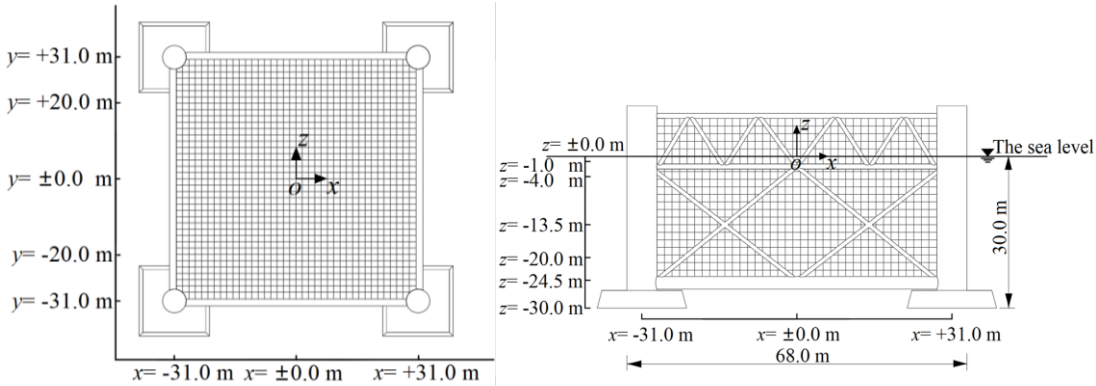

a. Vertical view b. Front view

Figure 12. The layout of the BFAF and the flow velocity monitoring plane.

3.1.1 Uniform flow

It is assumed that the flow velocity is uniform and constant, regardless of factors such as wind and waves. The flow field on the *x*-*y* plane along the incoming flow direction and the *y*-*z* plane along the vertical incoming flow direction are analyzed with the incident velocity of 1.20 m/s. The contours of the *x*-*y* plane at different depths are shown in Figure 13. The blocking effect of the BFAF on the flow velocity are obviously observed from the figure. Because of the complex configurations of the diagonal braces, vertical and horizontal columns, the velocity attenuations and the disturbed areas at different depths are different. Generally, the flow velocities inside and behind the aquacultural farm are greatly decreased. It also can be seen that the flow velocity at the upwind side slightly decreases due to the presence of nets and frame columns. It is noteworthy that the velocity reductions behind the BFAF continue for a long distance, at least twice the length of the aquacultural farm. In the transverse flow direction, the areas of the disturbed fluid are approximately the same as the width of the aquacultural farm. It is interesting to observe the trend in the flanks of the frame columns. The sudden increase in velocity occurs outside the frame column and decreases along the transverse flow direction. This phenomenon can be explained that the pressure energy is converted into the kinetic energy of the flow. Figure 14 shows the velocities along the center streamline (y=0) at different depths. As can be seen from the figure, the velocity extremes appear at the plane of the net. The flow velocity inside the aquacultural farm does not obviously change until reach the cage nets. No obvious trend of the flow velocity along the water depth direction inside the farm can be found due to the pile group effect. The velocities are attenuated in different degrees at different depths. For example, for the *x*-*y* plane at z= -24.5 m, the velocity near the upstream net increases sharply and then decreases due to the blocking effect of the net and the frame column. Inside the farm, the flow velocity is briefly restored. Behind the farm, the velocity is slowly recovered. As a contrast, the velocity at z= -4.0m is quite different from the z= -24.5 m plane. The continuous velocity decay occurs behind the farm at z= -4.0 m. The complex configurations of the trusses and columns contribute to the large different attenuations at different depths. The results suggest that not only the widely recognized block effect caused by nets should be considered, but also the complex columns and trusses have great influents on the flow characteristics.

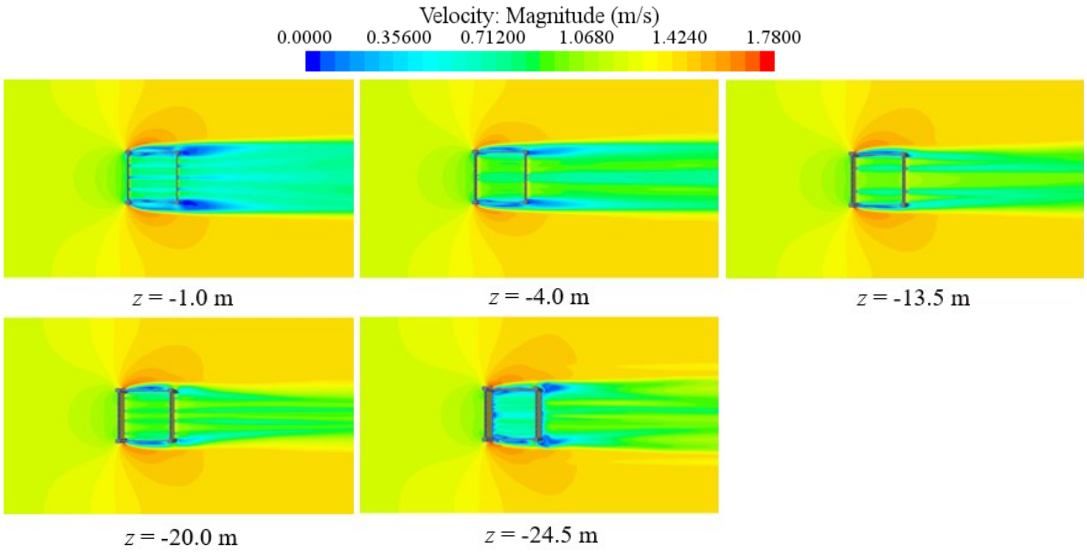

Figure 13. Contours of flow velocity on *x*-*y* plane at different depths.

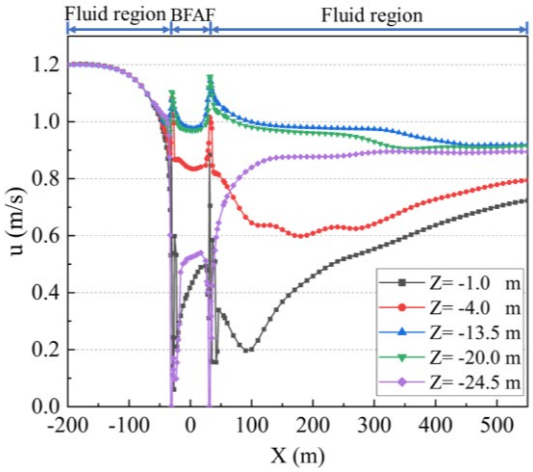

Figure 14. Variations of the flow velocity along the *x* directions at different depths at *y*=0 m.

To further clarify the regularity of the flow velocity inside the BFAF, Figure 15 shows the contour of the flow velocity on the *y*-*z* plane at *x*=0 m. It can be seen from the figure that the flow velocity obviously decreases from the farm to both sides. The average velocity inside the BFAF is lower than that around it. The velocity amplitude within the BFAF oscillates to a certain extent as shown in Figure 16. This is mainly due to the complexity of diagonal braces and fluid viscosity. It is noteworthy that a relatively large vibration is revealed at *z*= -24.5 m inside the BFAF. The phenomenon can be explained as the influence of fluid viscosity and bottom horizontal column. The results indicate that the flow velocities at different depths in the central region of the BFAF are uniformly distributed. It proves that suitable water exchange is carried on inside the BFAF to ensure the survival of fish.

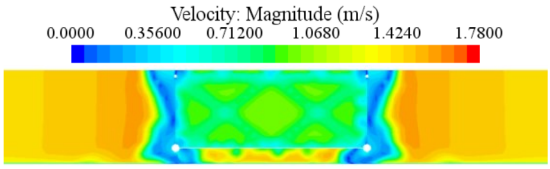

Figure 15. Contour of flow velocity on the *y*-*z* plane at *x*=0 m.

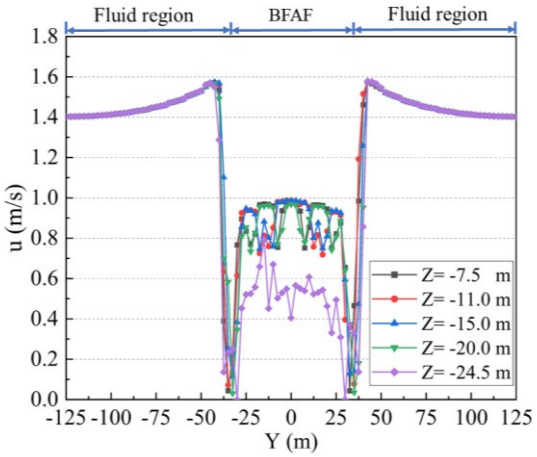

Figure 16 The magnitude of the flow velocity *u* along the *y*-direction at different depth.

3.1.2 Non-uniform flow velocity

The flow velocity is considered as the superposition of several velocity components in this section. The piecewise function is set to the velocity of the inlet boundary. Figure 17 displays the initial velocity distribution for non-uniform along the *z*-direction at the Inlet. As can be seen from the figure, the flow velocity is attenuated along the vertical direction. The velocity amplitude reaches a maximum at sea level, decreases with depth, and reaches a minimum near the seafloor. According to the 10th ISSC information on current ocean currents, the surface flow velocity U can be divided into the following parts:

$$U = U_t + U_w + U_s + U_m + U_{set-up} + U_d \tag{20}$$

where U_t is the tidal flow component, U_w is the component of the flow generated by the local wind, U_s is the component of the flow generated by the Stokes drift motion, U_m is the component of ocean circulation, $U_{set\text{-}up}$ is the component of the flow generated by the upwelling phenomenon and strong winds and waves, and U_d is the local water density-driven flow dominated by the strong water density fluctuation in the upper ocean.

The incident velocity of the non-uniform flow is superposed by the tidal flow component U_t and the local wind-generated flow component U_w. The above two components are related to water depth (Faltinsen, 1990), expressed as follows:

$$U_t(z)=\begin{cases} U_t(0), & -(h-10)\le z\le 0 \\ U_t(0)\log_{10}(1+\dfrac{9z}{10-h}), & -h<z<-(h-10) \end{cases} \tag{21}$$

$$U_w(z)=\begin{cases} U_w(0)\dfrac{(h_0+z)}{h_0}, & -h_0\le z\le 0 \\ 0, & z<-h_0 \end{cases} \tag{22}$$

where h is the water depth, h_0 is selected as 30.0m. In the initial estimation, $U_w(0)=0.02U_{10}$, U_{10} is the wind speed at 10.0m above sea level, which is set to 8.0m/s.

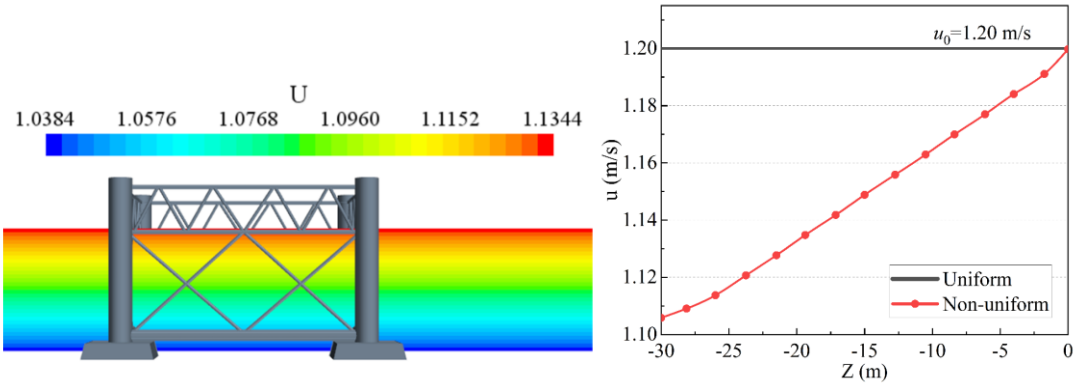

a. profile velocity contour b. profile velocity magnitude

Figure 17 Incident velocity distribution of non-uniform flow along the z direction at the Inlet.

To intuitively observe the difference between uniform and non-uniform flows in engineering analysis, the two working conditions are compared. The velocity amplitude of non-uniform flow at sea surface is set to be equal to uniform velocity. The velocity at the same section is compared to observe the difference between the two conditions. Figure 18 and Figure 19 show the contour of the flow velocity on the x-y plane and the magnitude of velocity at z= -13.5m plane. The plots show that the trend of non-uniform flow with the change of coordinates is basically consistent with uniform flow although the velocity decreases with the increase of the depth. It is noteworthy that it makes a fluctuation around x= 0 m in Figure 19. Before the upstream net, the flow velocity is gradually reduced due to the blocking effect of net and frame column. Some kinetic energy of the flow is converted into potential energy. The flow through the net from a higher surface caused a slight increase in flow velocity. This phenomenon of a small-scale jump is similar to that of hydraulic jump. Subsequently, the velocity is continuously attenuated by the blocking effect of the net and then gradually reaches stability. Figure 20 displays the contours of uniform and non-uniform flow velocities on the y-z plane at x=0 m. Two different flow velocity layers are shown in the figure. The comparison of flow velocity magnitudes for uniform and non-uniform flows is plotted in Figure 21. The maximum velocity magnitude difference between uniform and non-uniform is 26%, which occurs around y = ±15.0 m. The average relative difference is 4.96%,

which is higher than 1.70% in Figure 11b. The result demonstrates that the flow field characteristics caused by uniform and non-uniform flow are quite different inside the BFAF.

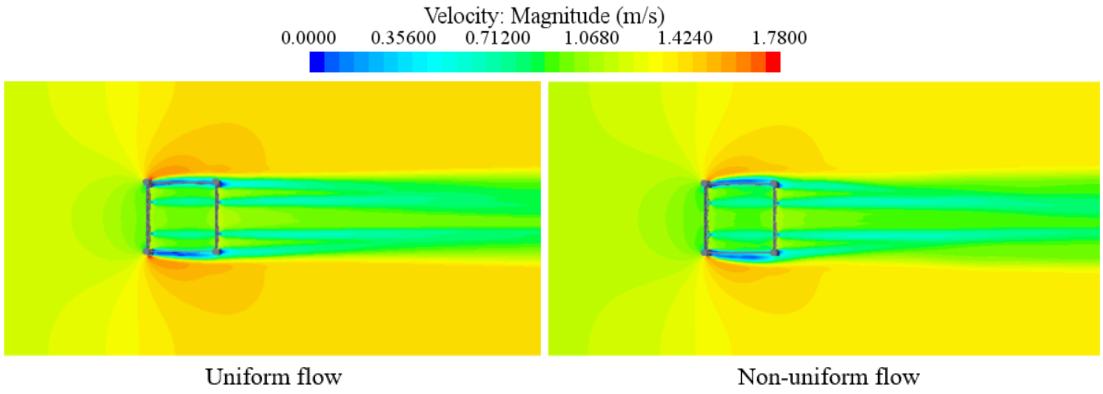

Figure 18. Contours of uniform and non-uniform flow velocities on the *x*-*y* plane along the *x*-direction.

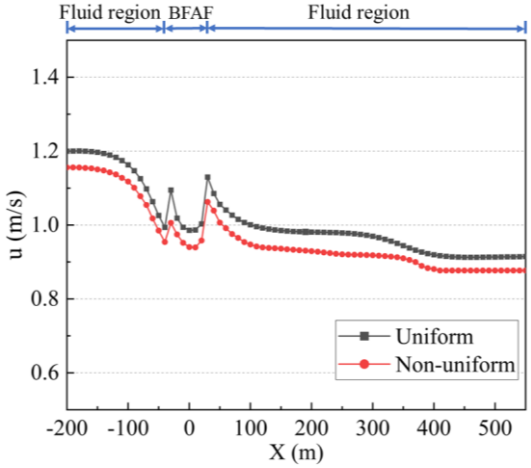

Figure 19. Comparison of flow velocity magnitudes for uniform and non-uniform flows along the *x* direction.

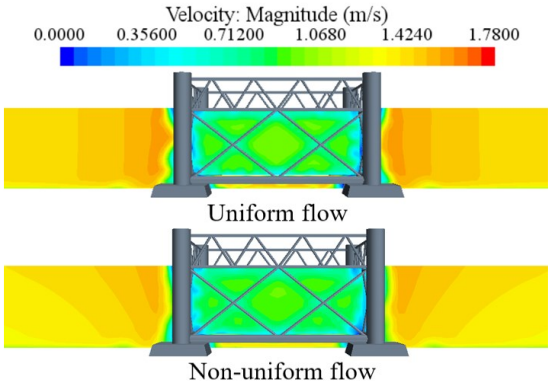

Figure 20. Contours of uniform and non-uniform flow velocities on the *y*-*z* plane along the *y*-direction.

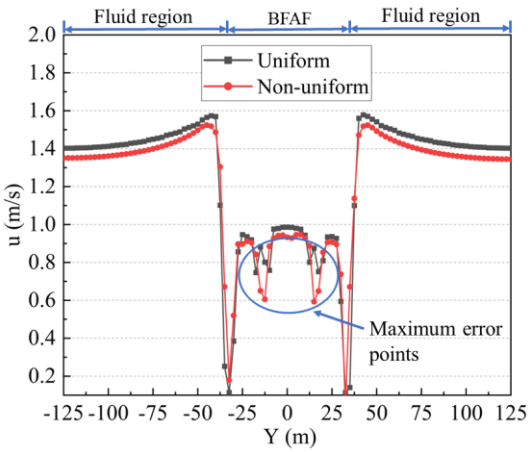

Figure 21. Comparison of flow velocity magnitudes for uniform and non-uniform flows along the *y* direction.

3.2 Effect of the angle of attack

To explore the influence of the flow angle, the flow field inside and around the BFAF at four different attack angles θ=0°, 15°, 30°, and 45° are analyzed. The flow field distribution along *x*-direction at *z*= -13.5 m plane at the four attack angles is shown in Figure 22a. It can be seen that the downstream flow velocity of the aquacultural farm with four attack angles has obvious attenuation. The flow field distributions on the *x*-*y* plane at 0° and 45° are symmetric about the central streamline *y*=0, whereas 15° and 30° are asymmetric. Figure 22b shows the flow field distribution of the *y*-*z* plane at *x*=0 m. It is effortless to notice that the flow velocity is high on the outside of the frame column, while almost zero across the frame column plane. In addition, the flow velocity is reduced at the locations where the truss columns exist, as can be seen from the light-colored locations in the figure.

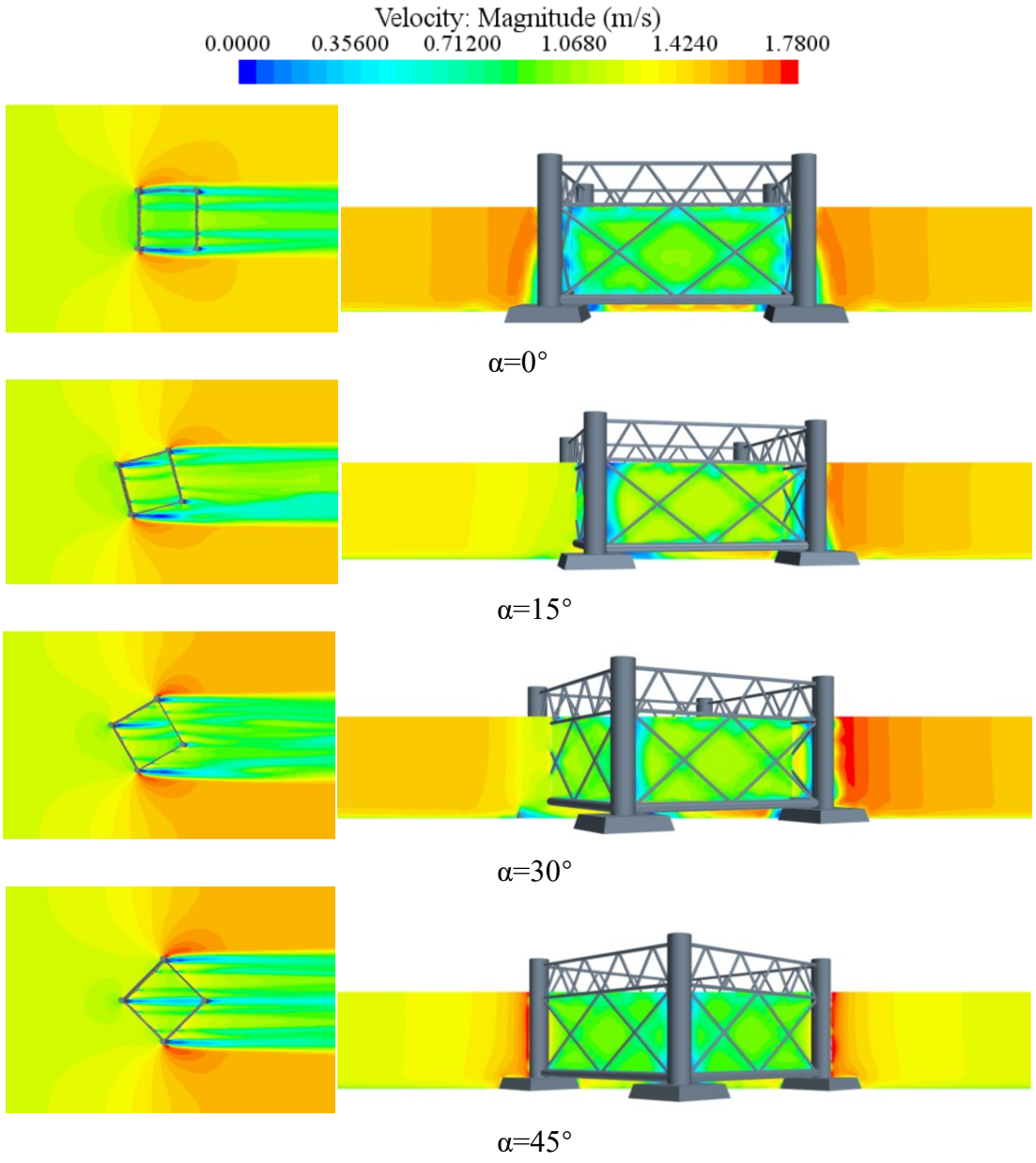

a. velocity along *x*-direction b. velocity along *y*-direction

Figure 22. Contours of flow velocity along the *x*-direction and the *y*-direction at different attack angles.

The dimensionless parameter-flow velocity attenuation factor $r=u/u_0$ is introduced to describe the flow velocity changes around the BFAF. u is the flow velocity at the measuring point, u_0 is the incoming flow velocity. The magnitudes of the flow velocity along the *x*-direction at the four attack angles are shown in Figure 23. The flow velocity distribution along the *x*-direction shows a trend of first decreasing and then increasing. A sharp decrease occurs at a particular point near the frame columns of the BFAF. With the increase of distance from the BFAF, the flow velocity roughly increases. At the three attack angles of α=15°, α=30° and α=45°, the influence range of the wake is significantly enlarged compared with the case of α=0°. The velocity reaches stable at 300 m downstream of the BFAF at the three attack

angles of α=15°, α=30° and α=45°. However, for the condition of α=0°, the velocity attenuation reaches stable at 100m downstream of the BFAF.

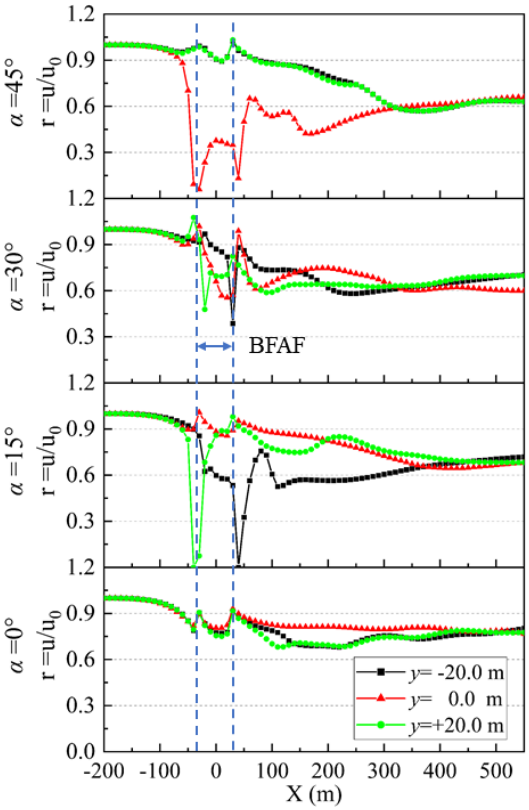

Figure 23. The magnitude of the flow velocity along the *x* direction for different angles at *z*= -13.5m plane. Legends represent the three straight lines *y*= -20.0m, *y*= 0.0m and *y*= 20.0m.

Comparisons of the velocity attenuation at four attack angles are shown in Figure 24. The average velocity of the three straight lines *y*= -20, 0, and 20m on the *x*-*y* plane inside the BFAF is calculated as shown in Table 1. To roughly quantify the velocity attenuations, the average flow velocity inside the farm is estimated. It can be concluded that the average velocity of the three attack angles of α=15°, 30°, and 45° is slightly lower than α=0°. The internal flow field becomes complicated with the existence of frame columns and nets in the BFAF. Variations in the angle of attack result in different spatial arrangements of the aquacultural farm frame cylinders. The complex interaction of the frame cylinders leads to the generation of a vortex. The high-velocity fluid produced by the vortex threatens the survival of fish. The detailed spatial and temporal distribution of vortex and velocity inside the aquacultural farm are suggested to be explored in further.

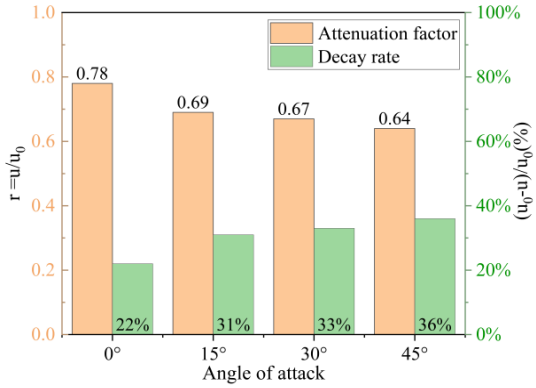

Figure 24. The attenuation of flow velocity at different angles of attack.

Table 1. The average flow velocity $\bar{\boldsymbol{u}}$ inside the aquacultural farm at four attack angles. u_1, u_2, and u_3 correspond to the average flow velocity of the three straight lines y=-20, 0, and 20 m within the aquacultural farm, respectively.

Inclination	u_1 (m/s)	u_2 (m/s)	u_3 (m/s)	$\bar{\boldsymbol{u}}$ (m/s)	r=u/u0
0°	0.965	0.995	0.949	0.970	0.81
15°	0.776	1.081	0.809	0.889	0.74
30°	1.002	0.890	0.765	0.886	0.73
45°	1.122	0.333	1.123	0.859	0.72

3.3 Effect of the solidity

For the fixed farm, the increasing biofouling are inevitable, which greatly affect the fish welfare and the pollutions distributions. To investigate the effect of solidity on the flow field around the nets, three net models with different solidities are analyzed in this section. Three representative solidities are selected: 0.130, 0.243 and 0.317. The three solidities and the corresponding resistances are given in Table 2. The small solidity S_1=0.130 represents the clear net without biofouling, which may lead to a slight blocking effect. The large solidity S_3=0.317 represents the small mesh nets and the highly biofouled nets. In fact, the net solidity is changed by factors such as the accumulation of fish excreta and marine organisms. The characteristics of the flow field for different net solidities at the incoming flow velocity u=1.20 m/s are investigated.

As shown in Figure 25, the x-y plane at z= -13.5 m and y-z plane at y=0 m are selected to observe the flow field characteristics. The velocity at the downstream of the farm with three different solidities is obviously attenuated. As expected, the flow velocity attenuation of solidity S_1 is the smallest, followed by S_2. The flow obstruction effect is significantly enhanced at solidity S_3. An increase in net solidity means a decrease in the net void area per unit area. The enhanced blocking effect of the net has an enlarged influence on the surrounding flow field. Therefore, it can be considered that the net solidity is a significant factor affecting the flow field around the aquacultural farm. Quantitative analysis of the flow field at three solidities is shown in Figure 26. The velocity attenuation factors corresponding to the S_1, S_2, and S_3 are 0.95, 0.80, and 0.67, respectively. The results indicate that the degree of velocity attenuation is positively correlated with the solidity of the net. As the distance from the aquacultural farm

increases, the downstream flow velocity tends to gradually increase. The solidity only changes the magnitude of the flow velocity without changing the flow trend. In subsequent studies, the effect of increasing solidity on the flow field over time will be explored.

Table 2. The porous resistance value for different solidities.

Solidity	Inertial resistance (kg/m^4)	Inertial tangential resistance (kg/m^4)	Viscous resistance ($kg/m^3 \cdot s$)	Viscous tangential resistance ($kg/m^3 \cdot s$)
S_1=0.130	1692.02	1021.31	112.81	34.52
S_2=0.243	3151.52	1442.48	153.52	37.47
S_3=0.317	6355.51	3369.02	849.60	106.43

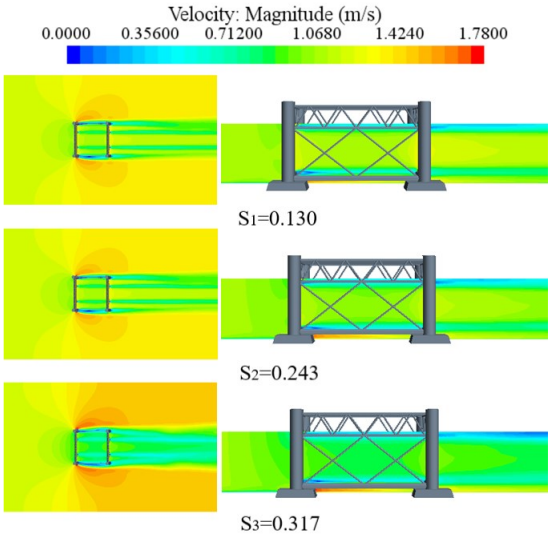

Figure 25. Contours of flow velocity on the *x*-*y* plane along the *x*-direction and the *y*-*z* plane at different solidities.

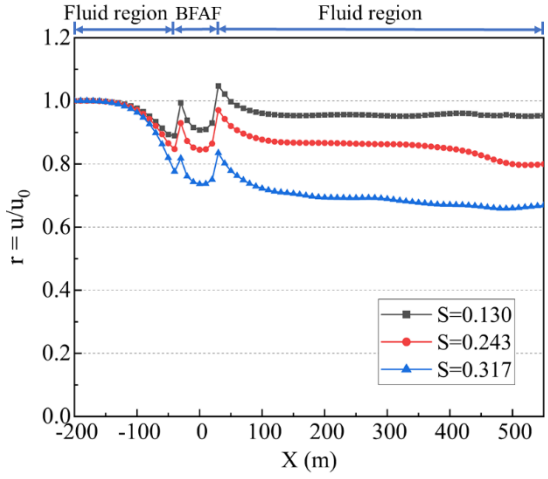

Figure 26. The magnitude of the flow velocity attenuation factor along the *x*-direction for three solidities.

4 Conclusions

This paper addresses the characteristics of the flow field inside and around the bottom-fixed aquacultural farm under the action of flow. The previous researches are concerned with traditional

floating net cages and pure nets, less research has been done on the flow field around large bottom-fixed deep-sea farms. In this study, the nets are established by the porous media model, the effect of the complex structure composed of columns and braces is considered. Therefore, the fluid morphology of the actual pasture can be more realistically reflected. Most of the existing studies have established numerical simulations at the model scale to explore the flow field characteristics, which has certain limitations compared with the prototype scale. The influence of different flow directions on the flow field is explored, which also provides a reliable basis for the arrangement of marine aquaculture farms. Based on the verified numerical model, the velocity distributions, the effects of velocity distribution, angle of attack, and net solidity on the BFAF are discussed in details. The main conclusions are as follows.

The results indicate that both the nets and the columns influent the flow velocity around the BFAF. The velocity attenuates in different degrees with depths, which is mainly caused by the complex configurations of trusses, vertical and horizontal columns. The finding tells us that the velocity at different depths and positions around the BFAF should be considered for the feeding decisions. It seems that the velocity distributions around the BFAF in non-uniform flows are generally more complex than in uniform flows. The velocity contour along the vertical and horizontal planes at different depths are quite different. Results demonstrate that different angles of attack give rise to different wake influence ranges. The average velocity attenuation of the aquacultural farm downstream is 33.3% for the three angles of attack α=15°, 30° and 45°. The angle of attack seems to lead to complicated vortex inside the aquacultural farm, which might influent the survival and activity of fish. It reminds us that the vortex mechanism inside the aquacultural farm should be paid much attention to. The effect of net solidity on the flow field inside and around the aquacultural farm is also investigated. The blocking effect is proportional to the solidity of the net. In practical engineering, the solidity is altered with fish excrement, residual bait, and marine organism. It is necessary not only to ensure adequate water exchange but also to maintain a suitable flow velocity. The net solidity should be checked regularly and the attachment of the net should be cleaned up in time.

The established numerical model studies the characteristics of the single BFAF in the flow. Although the porous media model provides a reasonable result of the fluid distribution of nets cages with large mount of meshes, the porous media model still has limitations. One is that the fluid-structure interaction of flexible nets is still difficult and time-consuming. Another is that because the details of the nets are not finely simulated, more accurate flow field information cannot be obtained. Furthermore, multiple aquacultural farms are placed in array to achieve higher economic benefits. The wake influence of the BFAF on the rear multiple farms should be further investigated, which might benefit the layout of the multiple farms. Another critical issue for the fixed aquacultural farm is the effect of the fish school on the flow and the pollutant particle distribution because of the less water change comparing with the

floating farm. The numerical simulation and the field measurement of the velocity and bait distributions for the BFAF are suggested in future research.

Acknowledge

The study is supported by the Open Foundation of State Key Laboratory of Coastal and Offshore Engineering of Dalian University of Technology [LP2006], National Natural Science Foundation of China [Grant No. 52101326, No.52101306 and No. 51979028], China Postdoctoral Science Foundation (Grant No. 2019M661024), Fundamental Research Funds for the Central Universities(Grant No. 3072022JC2701), National Science Foundation of Shandong Province (Grant No. ZR2021QE121), National Science Foundation of Heilongjiang Province (Grant No. LH2021E049).

Reference

Chu YI, Wang CM, Park JC, Lader PF, 2020. Review of cage and containment tank designs for offshore fish farming. Aquaculture 519, 734928.

Løland G, 1991. Current force on flow through fish farms. Ph.D. Dissertation, Norwegian Institute of Technology, Trondheim, Norway.

Forchheimer, P., 1901. Wasserbewegung durch boden, Zeitschrift des Vereines deutscher Ingenieure 45(50), 1781–8.

Bear, J., 1972. Dynamics of Fluids in Porous Media. America Elsevier Publishing Company, Inc, New York.

Anderson, J. D., Wendt, J, 1995. Computational Fluid Dynamics, McGraw Hill, New York.

Faltinsen, O. M., 1990. Sea loads on ships and offshore structures. Cambridge University Press, Cambridge.

Chen H, Christensen ED, 2017. Development of a numerical model for fluid-structure interaction analysis of flow through and around an aquaculture net cage. Ocean Engineering 142, 597-615.

Kristiansen T, Faltinsen OM, 2012. Modelling of current loads on aquaculture net cages. Journal of Fluids and Structures 34, 218-235.

Patursson Ø, Swift MR, Tsukrov I, Simonsen K, Baldwin K, Fredriksson D, Celikkol B, 2010. Development of a porous media model with application to flow through and around a net panel. Ocean Engineering 37, 314-324.

Menter FR, 1994. Two-equation eddy-viscosity turbulence models for engineering applications. AIAA Journal, 32, 1598-1605.

Xu Z, Qin H, 2020. Fluid-structure interactions of cage based aquaculture: from structures to organisms. Ocean Engineering 217, 107961.

567 Zhao YP, Liu HF, Bi CW, Cui Y, Guan CT. 2021. Numerical study on the flow field inside and
568 around a semi-submersible aquaculture platform. Applied Ocean Research 115, 102824.
569 Klebert P, Lader P, Gansel L, Oppedal F, 2013. Hydrodynamic interactions on net panel and
570 aquaculture fish cages: a review. Ocean Engineering 58, 260-274.
571 Bi CW, Zhao YP, Dong GH, Xu TJ, Gui FK. 2013. Experimental investigation of the reduction in
572 flow velocity downstream from a fishing net. Aquaucultrual Engineering 57, 71-81.
573 Zhao YP, Bi CW, Dong GH, Gui FK, Cui Y, Guan CT, Xu T, 2013a. Numerical simulation of the
574 flow around fishing plane nets using the porous media model. Ocean Engineering 62, 25-37.
575 Zhao YP, Bi CW, Dong GH, Gui FK, Cui Y, Xu T, 2013b. Numerical simulation of the flow field
576 inside and around gravity cages. Aquaucultrual Engineering 52, 1-13.
577 Bi CW, Zhao YP, Dong GH, 2020. Experimental study on the effects of farmed fish on the
578 hydrodynamic characteristics of the net cage. Aquaculture 524, 735239.
579 Bi CW, Zhao YP, Dong GH, Xu TJ, Gui FK, 2014. Numerical simulation of the interaction between
580 flow and flexible nets. Journal of Fluids and Structures 45, 180-201.
581 Gansel LC, Oppedal F, Birkevold J, Tuene SA, 2018. Drag forces and deformation of aquaculture
582 cages—full-scale towing tests in the field. Aquacultural Engineering 81, 46-56.
583 Martin T, Kamath A, Bihs H, 2020. A Lagrangian approach for the coupled simulation of fixed net
584 structures in a Eulerian fluid model. Journal of Fluids and Structures 94, 102962.
585 Martin T, Tsarau A, Bihs H, 2022. A numerical framework for modelling the dynamics of open
586 ocean aquaculture structures in viscous fluids. Applied Ocean Research, 106, 102410.